Carboxylate Anchors Act as Exciton Reporters in

1.3 nm Indium Phosphide Nanoclusters

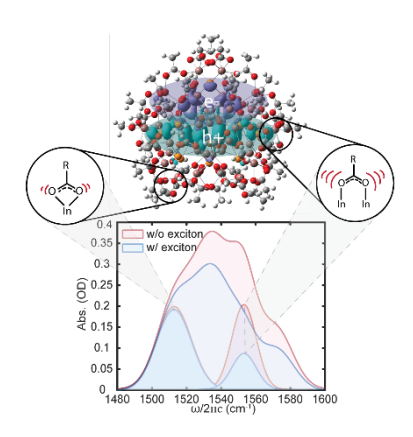
Joel D. Leger, Max R. Friedfeld, Ryan Beck, James D. Gaynor, Alessio Petrone[†], Xiaosong Li, Brandi M. Cossairt, and Munira Khalil*

Department of Chemistry, University of Washington, Seattle, Washington 98195, United States

KEYWORDS: quantum dot, InP, Ligand-nanoparticle coupling, tIR

ABSTRACT: Developing interfacial probes of ligand-nanocluster interactions is crucial for understanding and tailoring the optoelectronic properties of these emerging nanomaterials. Using transient-IR spectroscopy we demonstrate that ligand vibrational modes of oleate capped 1.3 nm InP nanoclusters report on the photogenerated exciton. The exciton induces an intensity change in the asymmetric carboxylate stretching mode by 57%, while generating no appreciable shift in frequency. Thus, the observed difference signal is attributed to an exciton induced change in the dipole magnitude of the asymmetric carboxylate stretching mode. Additionally, the transient-IR data reveals that the infrared dipole change is dependent on the geometry of the ligand bound to the nanocluster. The experimental results are interpreted using TDDFT calculations, which identify how the spatial dependence of an exciton-induced electron density shift affects the vibrational motion of the carboxylate anchors. More broadly, this work shows transient-IR spectroscopy as a useful method for characterizing ligand-nanocluster coupling interactions.

TOC GRAPHIC



The use of nanoparticles in the manufacturing of optoelectronics is gaining traction as a commercially viable strategy to improve the properties of common devices including wide color gamut displays, LEDs, and photovoltaics. The ability to easily tune their energy bandgaps, in addition to their solution processability and stability makes quantum dots (QDs) promising materials for these applications.¹⁻⁵ The optical properties of semiconductor nanoparticles are governed by both quantum confinement and surface effects. 6-8 The relative increase in surface atoms as the nanoparticle's volume decreases results in the surface chemistry playing a significant role in determining the excitonic properties of the nanoparticle, such as the charge carrier behavior. Typically, the surface of the nanoparticles are passivated using either a core-shell architecture or capping ligands to control the colloidal stability and optical properties of the nanoparticle.⁹⁻¹² Insulating, long chain fatty acids have proven to be effective capping ligands during initial solution phase synthesis due to their significant solubility in organic solvents. It is possible to modify the surface chemistry of nanoparticles post-synthetically through ligand exchange to control charge carrier dynamics, interparticle coupling, ¹³ and design additional functionality such as biochemical sensing capabilities. 14-15 The advances made in synthetically tuning the surface chemistry of nanoparticles are spurring the development of experimental probes to quantitatively understand how the ligand architecture mediates nanoparticle dynamics.

Nanoparticle capping ligands are effective at passivation due to their interaction with the facial atoms at the nanoparticle-ligand interface. The resulting interaction between the nanoparticle and the passivating ligands has motivated studies focusing on the ligands' effect on the nanoparticle wavefunction and the resultant band gap modification. Studies using a combination of X-ray photoelectron spectroscopy, pulsed cyclic voltammetry, and computational modeling have shown that the ligand effects on QD systems are nontrivial. Experiments on

PbS QDs measured modification in the valence band maximum (VBM) up to 2.0 eV when the ligands were functionalized with electron withdrawing groups of varying degrees. ¹⁹ A similar study done on CdSe QDs suggested the VBM shifts are also dependent on the nanoparticle size, where the smaller nanoparticles' wavefunction gains increased ligand character. ¹⁸ Indeed, the optical properties of CdSe nanoclusters with radii ≤1.2 nm were found to be significantly influenced by the ligand-exciton coupling. ²² Transient absorption spectroscopy has measured a ligand dependence on the band edge relaxation of CdSe QDs. ²³ These studies point to the importance of ligand-nanoparticle coupling and its effects on the overall nanoparticle exciton dynamics.

Several time-resolved spectroscopic studies have focused on understanding the role of low-frequency phonon modes in determining the pathways for free carrier relaxation dynamics. ²⁴⁻²⁹ In contrast, less work has been performed on elucidating the role of high-frequency vibrational modes of the capping ligands in ligand-nanoparticle coupling and exciton dynamics. ¹⁶ Since the nanoparticle wavefunction is influenced by ligand binding, the high-frequency vibrational modes of the ligand are also expected to play a role in the exciton dynamics. In addition to presenting a metric for ligand-nanocrystal coupling, the local nature of the high-frequency vibrational probes can also permit the extraction of site-specific information. Mixed-frequency, time-resolved techniques, like transient-IR (tIR) spectroscopy, are particularly well suited to probe ligand-exciton coupling dynamics. Work by Guyot-Sionnest and co-workers used IR spectroscopy to probe the influence of surface ligands in the intraband relaxation of CdSe nanocrystals. ³⁰⁻³² In addition, tIR measurements on PbS colloidal QDs were used to distinguish intraband vs trap-to-band transitions based on the presence of ligand carboxylate stretching vibrational signatures. ³³⁻³⁴ Time-dependent tIR measurements have also been applied to probe the kinetics of photoinduced

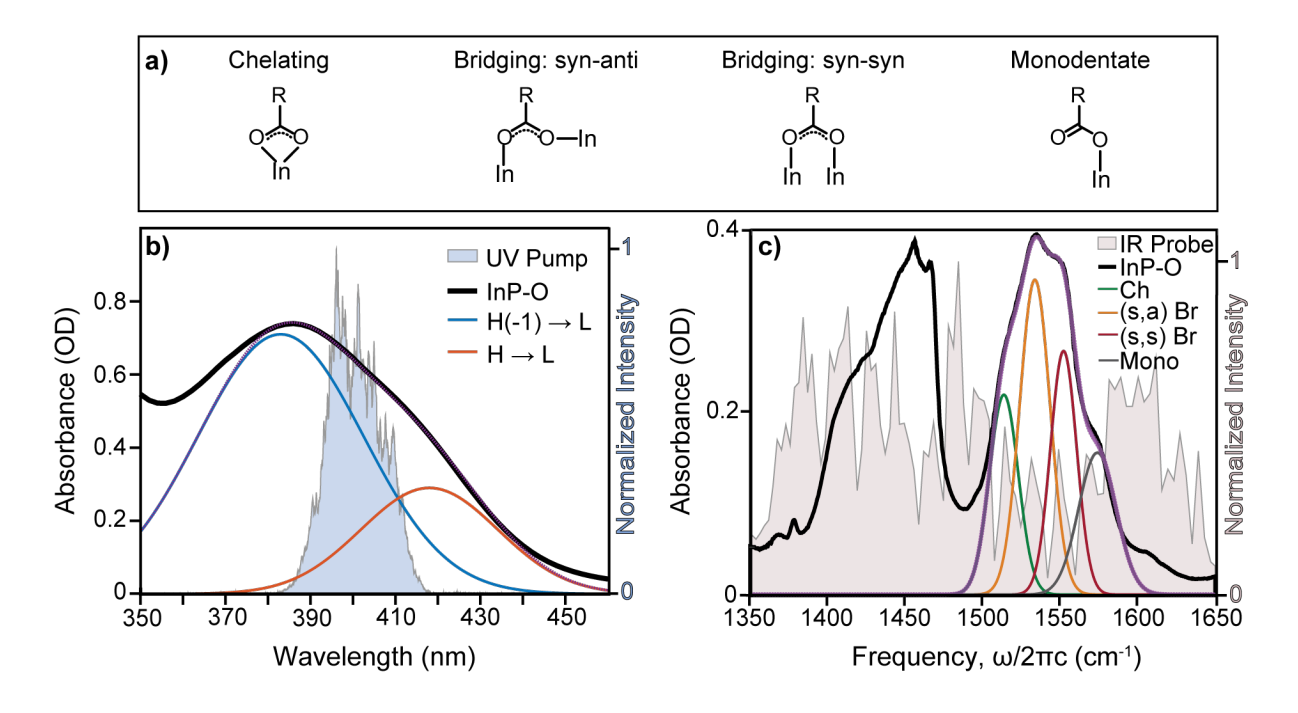


Figure 1. a) Schematic of different binding conformations found in metal-carboxylate anchors. b) UV/Vis of 0.8 mM 1.3 nm InP nanoclusters dissolved in tetrachloroethylene. The UV pump spectrum (blue area) overlaps with both the HOMO-1 to LUMO (blue line) and HOMO to LUMO (red line) of the nanocluster absorption spectrum (black line). c) FTIR spectrum of the nanocluster in the carboxylate region. The IR probe spectrum (red area) covers both the symmetric and asymmetric stretching vibrations (black line). The asymmetric region was fit to four peaks, associated with the different binding conformations present: chelating (green line), syn-anti bridging (orange line), syn-syn bridging (red line), and monodentate (gray line). The sum of the fits is shown as a purple line.

electron transfer at nanoparticle-ligand interfaces.³⁵⁻³⁶ These studies show the usefulness and potential of tIR as a way of observing excitonic behavior in QD systems.

In this study, we show that high-frequency carbonyl vibrations of the carboxylate ligand anchor give a unique response to exciton generation using tIR spectroscopy of an oleate-capped 1.3 nm InP nanocluster solution. Time-dependent density functional theory (TDDFT) calculations are used to help interpret the tIR data. At two picoseconds (ps) following exciton generation via UV photoexcitation, the changes in the carboxylate anchoring ligand vibrational spectrum show that one of the four ligand binding conformations, the syn-syn bridging motif (see Fig. 1a),

provides the strongest tIR response. The variation in the tIR signal response among the different carboxylate binding motifs reflects the spatial extent of the exciton at the nanocrystal surface. The observed high-frequency vibrational coupling to the exciton suggests that these vibrations need to be taken into account when considering non-radiative relaxation pathways in InP nanocrystals.

Previous characterization of the 1.3 nm InP nanocluster crystal structure capped with phenylacetate ligands showed that the carboxylate ligands bound to the surface indium atoms can assume various conformations (Figure 1a) with the following distribution: 24% chelating, 66% syn-anti bridging, 10% syn-syn bridging, and 0% in the monodentate form.³⁷ Analogous information can be extracted from the nanocluster solution by measuring and fitting the FTIR spectrum of the carboxylate stretching region of oleate-capped clusters (Figure 1c, black line). Since carboxylates contain large dipole moments, their vibrational stretching energies are subject to influences from environmental and structural changes. Several groups have taken advantage of the carboxylate's structural sensitivity to relate the measured stretching frequencies in the FTIR to that of specific binding conformations present in the system. 38-43 Work by Zelenak et al. used zinc(II) metal carboxylates to study the correlation of the O-C-O stretching frequencies with that of the carboxylate binding conformations.⁴³ Combining X-ray crystallography with FTIR data, they were able to assign the frequency separation between the carboxylate asymmetric and symmetric stretches, $\Delta \omega = \omega_{as}$ (COO-) - ω_{s} (COO-), and establish the following relationship: $\Delta\omega_{\text{chelating}} < \Delta\omega_{\text{(syn-anti)}}$ bridging $< \Delta\omega_{\text{(syn-syn)}}$ bridging $< \Delta\omega_{\text{monodentate}}$. Using this relationship, the FTIR spectral features in the carboxylate anchoring region of the InP nanoclusters can be assigned to specific binding conformations. The two main features centered around 1425 cm⁻¹ and 1540 cm⁻¹ are the O-C-O symmetric (1400 - 1475 cm⁻¹) and asymmetric (1500 - 1600 cm⁻¹) stretches, respectively. The substructure within each peak relates to the various binding conformations

assumed by the ligands. Unfortunately, deconvolution and assignment of the substructure in the symmetric stretching region proves difficult due to the additional presence of oleate CH₂ bending modes. For this reason, only the asymmetric stretching modes will be discussed here.

The line shape of the asymmetric carboxylate stretching mode was fit to four Gaussians corresponding to the four possible ligand conformations and the results are summarized in Table 1. Using the best fit results for the FTIR spectrum, we calculate a binding conformation distribution of 22±2 %, 45±2 %, 16±2 %, and 17±1 % for the chelating, syn-anti bridging, syn-syn bridging, and monodentate modes, respectively. This distribution deviates from the previously measured crystal structure, where the ligand binding confirmations were found to be 24% chelating, 66% syn-anti bridging, 10% syn-syn bridging, and 0% in the monodentate form.³⁷ The more evenly distributed ratio of binding motifs found by fitting the FTIR spectrum is most likely

TABLE I. Best-fit results obtained from fitting the asymmetric carboxylate stretching line shape in the ground state (GS) FTIR and photoexcited (ES) tIR spectrum to a sum of four Gaussian line shapes.

Conformation	Frequency, ω _c (cm ⁻¹)	Spectral Width, FWHM (cm ⁻¹)	Molar Absorption Coefficient in the Ground State, ϵ_{GS} (M ⁻¹ cm ⁻¹)	Molar Absorption Coefficient in the Photoexcited State, ε_{ES} (M ⁻¹ cm ⁻¹)	Change in the IR Transition Dipole Moment Upon Photoexcitation (% difference)*
Chelating	1513±1	23.6±1.4	659±39	635±55	4±8
Syn-Anti Bridging	1535±1	27±2	583±34	467±26	20±5
Syn-Syn Bridging	1553±0	16.6±0.4	934±55	396±93	57±10
Monodentate	1571±0	23.6±0.5	659±39	445±47	32±7

^{*}The measured % change is defined as $(\epsilon_{GS} - \epsilon_{ES})/\epsilon_{GS}$. Excited state values were extracted assuming 30.4 % of the molecules were excited.

a result of surface reorganization in solution, which is consistent with the dynamic nature of nanoparticle surfaces.⁴⁴

Figure 1b (black line) shows the optical absorption spectrum for the InP nanocluster. Previous work by Gary *et al.* observed that the optical absorption spectrum is a convolution of two electronic transitions.³⁷ A higher energy transition centered at 386 nm (Figure 1b, blue line) is assigned to the HOMO-1 to LUMO transition and a lower-lying transition centered at 418 nm (Figure 1b, red line) is assigned to the HOMO to LUMO transition. In order to carry out the tIR measurements, we excited the nanocluster, dissolved in tetrachloroethylene (TCE), with a laser pulse centered around 400 nm (Figure 1b, blue area). Under this condition, there is a probability of generating an exciton originating from either the HOMO-1 to LUMO or HOMO to LUMO. Because of this, we do not distinguish contributions between the two possible excitons. The IR probe has a bandwidth of 300 cm⁻¹ covering both the symmetric and asymmetric carboxylate stretching region (Figure 1c, red area).

Shown in Figure 2a is the resulting tIR differential absorption spectrum, collected at a two ps time delay to avoid solvent signal contributions and convolution with the instrument response. A detailed description of the experimental methods is provided in the Supplementary Information. The tIR spectrum in Figure 2a is representative of the vibrational response measured throughout the timescale of our measurements (Fig. S1). The measured t-IR signal intensity is linear with respect to the intensity of the pump-pulse (Fig. S6) and its lineshape is notably different from that obtained in a temperature-dependent FTIR study (Fig. S7).

Focusing on the line shape of the tIR signal shown in Figure 2a, we see a well-defined negative feature centered around 1552 cm⁻¹ along with a broader positive feature around 1425 cm⁻¹. Instinctively, one would assign the loss in absorption around 1552 cm⁻¹ to a ground state bleach

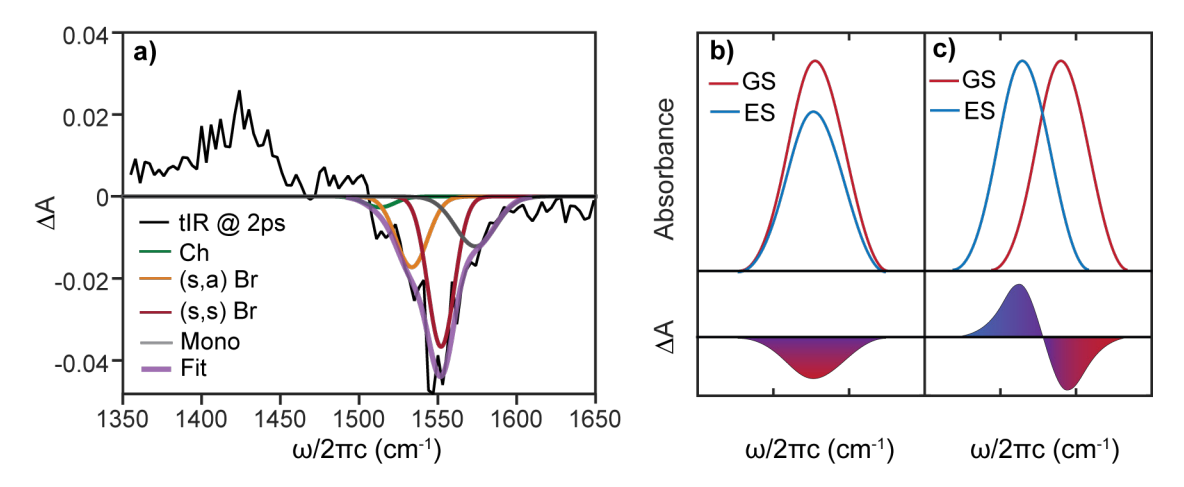


Figure 2. a) The tIR spectrum of InP nanoclusters dissolved in TCE taken at 2 ps following photoexcitation with the 400 nm pump pulse (black line). The fit of the carboxylate asymmetric stretching frequency at 2 ps following photoexcitation (purple line), consisting of a convolution of the four anchoring types' difference signal (colored lines), reports a reduction in the vibrational extinction coefficient upon exciton generation. Example tIR signals resulting from b) a change in extinction coefficient and c) change in central frequency following photoexcitation.

(GSB) and the new absorptive feature around 1425 cm⁻¹ to an excited state absorption (ESA). For this to be the case, the exciton would have to induce a frequency shift in the carboxylate stretching vibrations of more than 100 cm⁻¹. Such a large shift seems unreasonable considering that typical carboxylate frequency shifts of similar ligand-nanoparticle systems are between 5 to 20 cm⁻¹, following photoinduced electronic structural rearrangement (e.g., electron transfer).^{35, 45} Additionally, this frequency shift argument would require the tIR signal in the region between 1350 and 1450 cm⁻¹ to result from a convolution of the symmetric stretch GSB and the asymmetric stretch ESA, which is also unlikely given that the measured signal in the asymmetric and symmetric stretching region are of similar intensities.

Instead, we suggest that the observed signal intensity arises from changes in the dipole moment magnitudes of the carboxylate stretches for each bonding configuration (Figure 2b) following photoexcitation. Under this description, the observed loss in absorption at 1552 cm⁻¹

relates to an overall reduction in the extinction coefficient of the asymmetric carboxylate stretch and the increase in absorption around 1425 cm⁻¹ relates to an overall increase in the symmetric stretch extinction coefficient following photoexcitation. Following this description, the tIR difference spectrum was fit to the difference between the FTIR spectrum and the photoexcited nanocluster IR spectrum. This was done by constraining the central frequency and FWHM to the extracted values from the FTIR spectrum and floating the extinction coefficients of the photoexcited nanocluster IR spectrum. An additional 0.304 scalar (see SI) was applied to account for the fraction of nanoclusters excited (fits shown in Figure 2a, colored lines). The changes were found to be 4 ± 8 %, 20 ± 5 %, 57 ± 10 %, and 32 ± 7 % for the chelating, syn-anti bridging, syn-syn bridging, and monodentate dipoles respectively. The predominant feature, the syn-syn bridging conformation, experiences the largest change in extinction coefficient reducing by ~ 57 % in the presence of the exciton (Table 1). It is worth noting that these assignments hold true under the condition that all binding motifs have an equal probability of being excited.

In order to assign spectral features and interpret the nature of the tIR signal, the calculated IR spectra for both ground state and the first excited state optimized acetate-capped InP cluster geometries were calculated using TDDFT. Our calculations do not include vibronic coupling, which would require the use *ab initio* non adiabatic molecular dynamics methods that are currently computationally infeasible on a system of this size. It should be noted, however, that TDDFT is able to quantitatively predict the excited state intensities in the Franck-Condon region of the potential, which plays an important role in the generation of the ultrafast tIR response. We note that the acetate derivatives were used to save computational time. As it has been noted in previous investigations, differences in chain length do little to alter the geometric and electronic trends of the systems given that the In-O bond energy is mostly unchanged.^{44, 46} Given this, it is expected

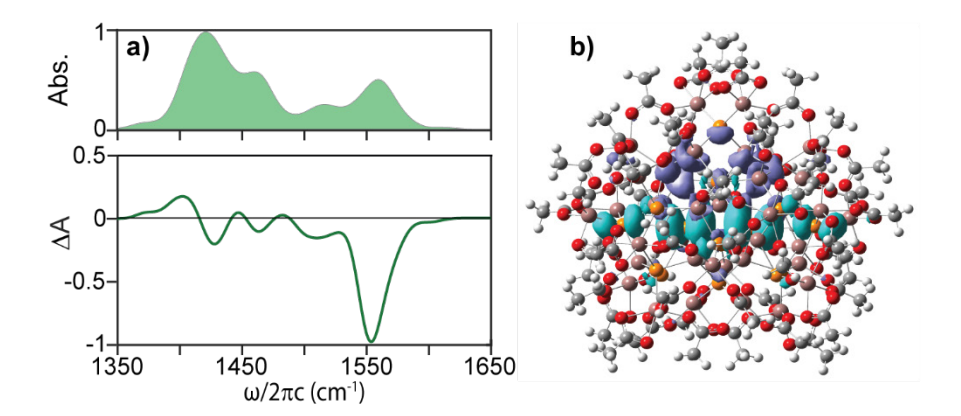


Figure 3. a) Harmonic frequency calculations of InP-Acetate nanoclusters using TDDFT. The calculate ground state IR spectrum is shown in the top panel, where the calculated difference spectrum between the excited state and ground state is shown in the bottom panel. All calculated frequencies are broadened by Gaussian line shapes with a 22 cm⁻¹ FWHM. See main text and SI for more details. b) Visualization of the shift in the electron density following HOMO to LUMO excitation in the InP nanocluster. The calculated natural transition orbital (NTO) shows electron density shifting away from the hole (teal volume) and localizes it to the excited electron (purple volume).

that the trends gleaned from the investigation of the vibrational spectra calculated with acetyl ligands will be applicable to systems with longer ligand chains. Additionally, due to the lack of π-bonding in alkanes, the chain length is expected to have little effect on the electronic structure of the nanocrystal. The calculated spectra were examined by identifying the modes contributing to the peaks in the ~1400-1600 cm⁻¹ carboxylate stretching region. As can be seen by the shaded green area in Figure 3a (top panel), there are two areas of interest in this energy region. Examination of the modes within these regions confirms that the ~1425 cm⁻¹ feature results from the symmetric O-C-O carboxylate stretching of the acetate ligands capping the InP core, while the ~1552 cm⁻¹ feature consists of asymmetric O-C-O stretching. Further examination of these two features also confirms that the trends in the carboxylate stretching frequencies described above match with the four ligand binding conformations in these oleate-capped InP (See Fig. S2 in the SI). The photoexcited nanocluster IR difference spectrum (Figure 3a, bottom panel) has a

noticeable decrease of intensity in the asymmetric stretching frequency region, which is consistent with the experimentally observed tIR measurements at a two ps time delay. The calculations also show a slight increase in the intensity of the symmetric stretching frequency for the photoexcited InP nanocluster, which is less consistent with the experimentally observed results. This discrepancy could arise from the difference in chain length of the ligands used in the experiment and the calculations because the calculated vibrational spectrum does not include the same extent of alkyl CH₂ bending modes that convolute the carboxylate symmetric stretching region.

There are two main factors that affect the calculated photoexcited nanocluster IR spectrum. The optimized excited state geometry undergoes a slight lattice distortion when compared to the ground state.⁴⁷ The lattice shift is seen in the calculations as an expansion along the southern hemisphere of the nanocluster, most likely due to the shift in electron density during exciton formation (Figure 3b). A portion of the anchoring ligands undergo small energy shifts while others are unchanged upon photoexcitation. The more significant effect seen in the calculations is a change in the dipole moment corresponding to the vibrational modes. This is most evident for the syn-syn bridging normal mode found at 1556 cm⁻¹, whose intensity decreases by 52 % upon photoexcitation without any significant change in its vibrational frequency (Fig. S4 in the SI). The ligand's vibrational response can be understood by the spatial relationship between the surfacebound ligands and the facial atoms affected by the shift in electron density due to exciton generation. The InP nanocluster exciton gives rise to a hole localized along the longitudinal axis (Figure 3b, teal volume), and redistributes the electron towards the northern hemisphere of the nanocluster (Figure 3b, purple volume). Highlighting the ligands with 1556 cm⁻¹ asymmetric stretching normal modes within the calculated InP frame shows that a large quantity of these ligands reside along the axis of electron density shift (Fig. S3 in the SI). These observations

provide strong evidence that the electron density shift in relation to the vibrational coordinate induces a change in the transition dipole moment of the vibrational mode with minimal effect to the vibrational force constant.

While low-frequency phonon modes have proven important to the energy relaxation dynamics in many nanomaterials, our study highlights how the high-frequency vibrational modes of the ligand can also be relevant for the electronic properties of the nanomaterial. In the InP nanocluster, the coupling between the high-frequency carboxylate stretching vibrations of the ligand anchoring group and the excitonic transition could lead to the nonradiative dissipation of excess electronic energy. The results reported here are generally in agreement with recent surface sensitive sum-frequency generation experiments on ligand-nanoparticle assemblies where excitonvibrational dipolar interactions were found to be a significant interaction mechanism between the ligand and the nanoparticle.⁴⁸ Our work demonstrates how the high-frequency vibrational features from the ligand provide a spectroscopic handle that can be sensitive to binding conformation distributions, changes to the nanoparticle surface environment, and spatially localized fluctuations in electron density due to exciton generation. The tIR measurements on oleate-capped InP nanoclusters reported here show an immediate carboxylate vibrational signal upon photoexcitation with a distinct, conformation-dependent intensity profile. The experimental spectra indicate that ligand vibrational transition dipole moments can change dramatically (greater than 50 % for the syn-syn conformation) due to the proximity between the ligand anchoring group and the exciton. While couplings between an exciton and ligand vibrations are widely reported, an in-depth experimental characterization of the exciton's perturbation to the ligand has not been reported until now – that is, in terms of distinguishing between frequency shifting and changes in dipole magnitude of the ligand vibration.

The tIR results reported here demonstrate the potential for new avenues of characterizing

nanoparticles through direct observation of the ligand's vibrational response to exciton dynamics

as a function of core-shell architectures and ligand functionalization. We note that in larger

nanoparticles, there will be increased complexity in signal interpretation because the tIR response

of the anchoring groups and other reporters could be convoluted with the intraband transitions.³³

Since the ligand vibrations are sensitive to shifts in electron density, tIR spectroscopy allows for

the possibility to track localized carrier states through time-dependent variations in the ligand

anchoring modes of the photoexcited nanocrystal. Additional vibrational tags placed along ligand

scaffolding would further permit the ability to track local exciton dynamics beyond the

nanoparticle surface. This work lays the foundation for future transient IR experiments designed

to provide a deeper understanding of the ligand-nanocrystal interactions.

ASSOCIATED CONTENT

Supporting Information. The Supporting Information is available free of charge on the ACS

Publications website. Experimental details of tIR measurements, synthesis, and parameters used

in TD-DFT. Figures of time-dependent tIR measurements, plots of the calculations: freq. vs

intensity and a heat map for the normal mode centered at 1556 cm⁻¹. (PDF)

AUTHOR INFORMATION

Corresponding Author

*E-mail: mkhalil@uw.edu.

Present Address:

14

[†]AP: Dipartimento di Scienze Chimiche, Università degli Studi di Napoli Federico II, Complesso

Universitario di Monte S. Angelo, via Cintia 21, 80126 Napoli, Italy

ORCID

Joel Leger: 0000-0003-1068-7734

James Gaynor: 0000-0001-5253-8142

Alessio Petrone: 0000-0003-2232-9934

Xiaosong Li: 0000-0001-7341-6240

Brandi M. Cossairt: 0000-0002-9891-3259

Munira Khalil: 0000-0002-6508-4124

Notes

The authors declare no competing financial interest.

ACKNOWLEDGEMENTS

M.K. and J.D.L. acknowledge funding from the National Science Foundation (CHE-1565759).

B.M.C. acknowledges funding from the National Science Foundation (CHE-1552164). X.L.

acknowledges funding from the National Science Foundation (CHE-1565520). M.R.F

acknowledges the Washington Research Foundation for fellowship support. J.D.G. is supported

by the NSF GRFP, Division of Graduate Education (No. DGE-1256082). R.B. was supported by

the University of Washington Molecular Engineering Materials Center funded by the National

Science Foundation (DMR-1719797). This work was facilitated by advanced computational,

storage, and networking infrastructure provided by the Hyak supercomputer system at University

of Washington, funded by the Student Technology Fee.

15

REFERENCES

- 1. Kamat, P. V., Quantum Dot Solar Cells. The Next Big Thing in Photovoltaics. *J. Phys. Chem. Lett.* **2013**, *4* (6), 908-18.
- 2. Purcell-Milton, F.; Gun'ko, Y. K., Quantum dots for Luminescent Solar Concentrators. *J. Mat. Chem.* **2012**, *22* (33), 16687.
- 3. Talapin, D. V.; Lee, J. S.; Kovalenko, M. V.; Shevchenko, E. V., Prospects of colloidal nanocrystals for electronic and optoelectronic applications. *Chem. Rev.* **2010**, *110* (1), 389-458.
- 4. Resch-Genger, U.; Grabolle, M.; Cavaliere-Jaricot, S.; Nitschke, R.; Nann, T., Quantum dots versus organic dyes as fluorescent labels. *Nat. Methods* **2008**, *5* (9), 763-775.
- 5. Sun, Q.; Wang, Y. A.; Li, L. S.; Wang, D.; Zhu, T.; Xu, J.; Yang, C.; Li, Y., Bright, multicoloured light-emitting diodes based on quantum dots. *Nat. Photonics* **2007**, *1* (12), 717-722.
- 6. Lieber, C. M., One-dimensional nanostructures: Chemistry, physics & applications. *Solid State Commun.* **1998**, *107* (11), 607-616.
- 7. Alivisatos, A. P., Semiconductor clusters, nanocrystals, and quantum dots. *Science* **1996**, *271* (5251), 933-937.
- 8. Peterson, M. D.; Cass, L. C.; Harris, R. D.; Edme, K.; Sung, K.; Weiss, E. A., The Role of Ligands in Determining the Exciton Relaxation Dynamics in Semiconductor Quantum Dots. *Ann. Rev. Phys. Chem.* **2014**, *65* (1), 317-339.

- 9. Hendricks, M. P.; Campos, M. P.; Cleveland, G. T.; Jen-La Plante, I.; Owen, J. S., NANOMATERIALS. A tunable library of substituted thiourea precursors to metal sulfide nanocrystals. *Science* **2015**, *348* (6240), 1226-30.
- 10. Gary, D. C.; Terban, M. W.; Billinge, S. J. L.; Cossairt, B. M., Two-Step Nucleation and Growth of InP Quantum Dots via Magic-Sized Cluster Intermediates. *Chem. Mat.* **2015**, 27 (4), 1432-1441.
- 11. Munro, A. M.; Jen-La Plante, I.; Ng, M. S.; Ginger, D. S., Quantitative Study of the Effects of Surface Ligand Concentration on CdSe Nanocrystal Photoluminescence. *J. Phys. Chem. C* **2007**, *111* (17), 6220-6227.
- 12. Jeong, S.; Achermann, M.; Nanda, J.; Ivanov, S.; Klimov, V. I.; Hollingsworth, J. A., Effect of the thiol-thiolate equilibrium on the photophysical properties of aqueous CdSe/ZnS nanocrystal quantum dots. *J. Am. Chem. Soc.* **2005**, *127* (29), 10126-7.
- 13. Talapin, D. V.; Murray, C. B., PbSe nanocrystal solids for n- and p-channel thin film field-effect transistors. *Science* **2005**, *310* (5745), 86-9.
- 14. Michalet, X.; Pinaud, F. F.; Bentolila, L. A.; Tsay, J. M.; Doose, S.; Li, J. J.; Sundaresan, G.; Wu, A. M.; Gambhir, S. S.; Weiss, S., Quantum dots for live cells, in vivo imaging, and diagnostics. *Science* **2005**, *307* (5709), 538-44.
- 15. Pujari, S. P.; Scheres, L.; Marcelis, A. T.; Zuilhof, H., Covalent surface modification of oxide surfaces. *Angewandte Chemie* **2014**, *53* (25), 6322-56.

- 16. Lifshitz, E., Evidence in Support of Exciton to Ligand Vibrational Coupling in Colloidal Quantum Dots. *J. Phys. Chem. Lett.* **2015**, *6* (21), 4336-47.
- 17. Swenson, N. K.; Ratner, M. A.; Weiss, E. A., Computational Study of the Resonance Enhancement of Raman Signals of Ligands Adsorbed to CdSe Clusters through Photoexcitation of the Cluster. *J. Phys. Chem. C* **2016**, *120* (37), 20954-20960.
- 18. Bloom, B. P.; Zhao, L.-B.; Wang, Y.; Waldeck, D. H.; Liu, R.; Zhang, P.; Beratan, D. N., Ligand-Induced Changes in the Characteristic Size-Dependent Electronic Energies of CdSe Nanocrystals. *J. Phys. Chem. C* **2013**, *117* (43), 22401-22411.
- Kroupa, D. M.; Voros, M.; Brawand, N. P.; McNichols, B. W.; Miller, E. M.; Gu, J.; Nozik,
 A. J.; Sellinger, A.; Galli, G.; Beard, M. C., Tuning colloidal quantum dot band edge positions through solution-phase surface chemistry modification. *Nat. Commun.* 2017, 8, 15257.
- 20. Frederick, M. T.; Amin, V. A.; Weiss, E. A., Optical Properties of Strongly Coupled Quantum Dot-Ligand Systems. *J. Phys. Chem. Lett.* **2013**, *4* (4), 634-40.
- Giansante, C., Surface Chemistry Control of Colloidal Quantum Dot Band Gap. J. Phys.
 Chem. C 2018, 122 (31), 18110-18116.
- 22. Jethi, L.; Mack, T. G.; Kambhampati, P., Extending Semiconductor Nanocrystals from the Quantum Dot Regime to the Molecular Cluster Regime. *J. Phys. Chem. C* 2017, 121 (46), 26102-26107.

- 23. Schnitzenbaumer, K. J.; Labrador, T.; Dukovic, G., Impact of Chalcogenide Ligands on Excited State Dynamics in CdSe Quantum Dots. *J. Phys. Chem. C* **2015**, *119* (23), 13314-13324.
- Janke, E. M.; Williams, N.; She, C.; Zherebetskyy, D.; Hudson, M.; Wang, L.; Gosztola,
 D. J.; Schaller, R. D.; Lee, B.; Sun, C.; Engel, G. S.; Talapin, D. V., The origin of broad emission spectra in InP quantum dots: contributions from structural and electronic disorder.
 J. Am. Chem. Soc. 2018, 140 (46), 15791-15803.
- Dong, S.; Trivedi, D.; Chakrabortty, S.; Kobayashi, T.; Chan, Y.; Prezhdo, O. V.; Loh, Z.
 H., Observation of an Excitonic Quantum Coherence in CdSe Nanocrystals. *Nano Lett.*2015, 15 (10), 6875-82.
- 26. Baker, J. A.; Kelley, D. F.; Kelley, A. M., Resonance Raman and photoluminescence excitation profiles and excited-state dynamics in CdSe nanocrystals. *J. Chem. Phys.* **2013**, *139* (2), 024702.
- Yazdani, N.; Bozyigit, D.; Vuttivorakulchai, K.; Luisier, M.; Infante, I.; Wood, V., Tuning Electron-Phonon Interactions in Nanocrystals through Surface Termination. *Nano Lett.* 2018, 18 (4), 2233-2242.
- Caram, J. R.; Zheng, H.; Dahlberg, P. D.; Rolczynski, B. S.; Griffin, G. B.; Dolzhnikov,
 D. S.; Talapin, D. V.; Engel, G. S., Exploring size and state dynamics in CdSe quantum dots using two-dimensional electronic spectroscopy. *J. Chem. Phys.* 2014, 140 (8), 084701.

- 29. Kobayashi, Y.; Chuang, C.-H.; Burda, C.; Scholes, G. D., Exploring Ultrafast Electronic Processes of Quasi-Type II Nanocrystals by Two-Dimensional Electronic Spectroscopy. *J. Phys. Chem. C* **2014**, *118* (29), 16255-16263.
- 30. Guyot-Sionnest, P.; Hines, M. A., Intraband transitions in semiconductor nanocrystals. *Appl. Phys. Lett.* **1998,** 72 (6), 686-688.
- 31. Guyot-Sionnest, P.; Shim, M.; Matranga, C.; Hines, M., Intraband relaxation in CdSe quantum dots. *Phys. Rev. B* **1999**, *60* (4), R2181-R2184.
- 32. Guyot-Sionnest, P.; Wehrenberg, B.; Yu, D., Intraband relaxation in CdSe nanocrystals and the strong influence of the surface ligands. *J. Chem. Phys.* **2005**, *123* (7), 074709.
- 33. Tang, J.; Kemp, K. W.; Hoogland, S.; Jeong, K. S.; Liu, H.; Levina, L.; Furukawa, M.; Wang, X.; Debnath, R.; Cha, D.; Chou, K. W.; Fischer, A.; Amassian, A.; Asbury, J. B.; Sargent, E. H., Colloidal-quantum-dot photovoltaics using atomic-ligand passivation. *Nat. Materials* **2011**, *10* (10), 765-71.
- 34. Jeong, K. S.; Tang, J.; Liu, H.; Kim, J.; Schaefer, A. W.; Kemp, K.; Levina, L.; Wang, X.; Hoogland, S.; Debnath, R.; Brzozowski, L.; Sargent, E. H.; Asbury, J. B., Enhanced mobility-lifetime products in PbS colloidal quantum dot photovoltaics. ACS Nano 2012, 6 (1), 89-99.
- 35. Brown-Xu, S. E.; Chisholm, M. H.; Durr, C. B.; Gustafson, T. L.; Spilker, T. F., Photophysical Properties of cis-Mo₂ Quadruply Bonded Complexes and Observation of

- Photoinduced Electron Transfer to Titanium Dioxide. *J. Am. Chem. Soc.* **2014,** *136* (32), 11428-35.
- 36. Asbury, J. B.; Hao, E. C.; Wang, Y. Q.; Lian, T. Q., Bridge Length-Dependent Ultrafast Electron Transfer from Re Polypyridyl Complexes to Nanocrystalline TiO₂ Thin Films Studied by Femtosecond Infrared Spectroscopy. *J Phys Chem B* **2000**, *104* (50), 11957-11964.
- 37. Gary, D. C.; Flowers, S. E.; Kaminsky, W.; Petrone, A.; Li, X.; Cossairt, B. M., Single-Crystal and Electronic Structure of a 1.3 nm Indium Phosphide Nanocluster. *J. Am. Chem. Soc.* **2016**, *138* (5), 1510-3.
- 38. Jovanović, S.; Spreitzer, M.; Tramšek, M.; Trontelj, Z.; Suvorov, D., Effect of Oleic Acid Concentration on the Physicochemical Properties of Cobalt Ferrite Nanoparticles. *J. Phys. Chem. C* **2014**, *118* (25), 13844-13856.
- 39. Chernyshova, I. V.; Ponnurangam, S.; Somasundaran, P., Adsorption of Fatty Acids on Iron (Hydr)Oxides from Aqueous Solutions. *Langmuir* **2011**, *27* (16), 10007-18.
- 40. Cros-Gagneux, A.; Delpech, F.; Nayral, C.; Cornejo, A.; Coppel, Y.; Chaudret, B., Surface Chemistry of InP Quantum Dots: a Comprehensive Study. *J. Am. Chem. Soc.* **2010,** *132* (51), 18147-57.
- 41. Wu, N.; Fu, L.; Su, M.; Aslam, M.; Wong, K. C.; Dravid, V. P., Interaction of Fatty Acid Monolayers with Cobalt Nanoparticles. *Nano Lett.* **2004**, *4* (2), 383-386.

- 42. Lee, S. J.; Han, S. W.; Choi, H. J.; Kim, K., Structure and Thermal Behavior of a Layered Silver Carboxylate. *J. Phys. Chem. B* **2002**, *106* (11), 2892-2900.
- 43. Zelenak, V.; Vargova, Z.; Gyoryova, K., Correlation of Infrared Spectra of Zinc(II) Carboxylates with their Structures. *Spectrochimica Acta. A* **2007**, *66* (2), 262-72.
- 44. Zhao, Q.; Kulik, H. J., Electronic Structure Origins of Surface-Dependent Growth in III–V Quantum Dots. *Chem. Mat.* **2018**, *30* (20), 7154-7165.
- 45. Brown-Xu, S. E.; Chisholm, M. H.; Durr, C. B.; Lewis, S. A.; Spilker, T. F.; Young, P. J., Mo₂ Paddlewheel Complexes Functionalized With a Single MLCT, S₁ Infrared-Active Carboxylate Reporter Ligand: Preparation and Studies of Ground and Photoexcited States. *Inorg. Chem.* **2014**, *53* (1), 637-44.
- 46. Xie, L.; Zhao, Q.; Jensen, K. F.; Kulik, H. J., Direct Observation of Early-Stage Quantum Dot Growth Mechanisms with High-Temperature Ab Initio Molecular Dynamics. *J. Phys. Chem. C* **2016**, *120* (4), 2472-2483.
- 47. Stein, J. L.; Steimle, M. I.; Terban, M. W.; Petrone, A.; Billinge, S. J. L.; Li, X.; Cossairt, B. M., Cation Exchange Induced Transformation of InP Magic-Sized Clusters. *Chem. Mat.* **2017**, *29* (18), 7984-7992.
- 48. Noblet, T.; Dreesen, L.; Boujday, S.; Méthivier, C.; Busson, B.; Tadjeddine, A.; Humbert, C., Semiconductor Quantum Dots Reveal Dipolar Coupling from Exciton to Ligand Vibration. *Commun. Chem.* **2018**, *1* (1).

Supplementary Information to Accompany:

Carboxylate Anchors Act as Exciton Reporters in 1.3 nm Indium Phosphide Nanoclusters.

Joel D. Leger, Max R. Friedfeld, Ryan Beck, James D. Gaynor, Alessio Petrone, Xiaosong Li, Brandi M. Cossairt, and Munira Khalil*

Department of Chemistry, University of Washington, Seattle, Washington 98195, United States *Corresponding Author: mkhalil@uw.edu

METHODS.

Calculation of Fraction of Nanoclusters Excited. The fraction (fr) of nanoparticles that were excited by the electric field: $fr = \frac{\# of \ photons \ absorbed}{\# of \ nanoparticles \ in \ beam \ path}$, where the $\# of \ photons \ absorbed$ is found from the UV/Vis Spectrum and laser power at the sample. The $\# of \ nanoparticles \ in \ beam \ path$ is found from the concentration and volume, where the sample volume illuminated by the laser is considered to be cylindrical. Using the UV/Vis spectrum and pulse energy it was found that the sample absorbs 2.74×10^{12} photons per pulse dividing this value by the number of nanoclusters in the beam path, 9.01×10^{12} , results in .3037 of the total nanoclusters being excited.

Nanocluster Synthesis. The InP clusters with oleate carboxylate ligands were synthesized using the reported literature procedure, substituting oleic acid (OA) for myristic acid.² The procedure has been expanded into a video report of the synthesis.³

<u>Linear Spectra</u>. All linear spectra were collected using 0.8 mmol concentration of InP-OA dissolved in tetrachloroethylene (TCE) in a static sample cell with a 300 µm Teflon spacer between

two CaF₂ windows. The sample's exposure to air was limited to the time it took to transfer the solution into the static sample cell. FTIR data was collected on a Jasco FT/IR-4100A with a 1 cm⁻¹ resolution. A solvent subtraction was performed due to TCE containing spectral content between 1350 and 1650 cm⁻¹. UV/Vis data was collected in Jasco V-630 with a resolution of 2 nm.

Transient IR (tIR) Measurements. The tIR spectra were collected under the same concentration and solvent as the linear measurements. In order to prevent photo damage, the sample was flowed using a closed system peristaltic pump and the sample cell raster-scanned every 10 seconds. The tIR setup was performed using a Mai Tai oscillator and Spitfire Pro XP regenerative amplifier (Spectra Physics, output specs: 1 kHz rep rate, 35 fs pulse duration, 4.0 W output centered at 800 nm) resulting in an IRF of 200 fs. Before generating the 400 nm pump beam with a 200 μm BBO, the 800 nm fundamental was broadened via three 140μm (BK7) windows. The second harmonic of this broadened fundamental allowed for a broadened tunable pump beam between 385 nm to 415 nm, with a 17 nm (FWHM) bandwidth. The mid-IR probe pulse was generated using an inhouse built optical parametric amplifier and difference frequency generation setup. The pump and probe intensities were 1.5 μJ/pulse and 500 nJ/pulse, respectively; pump fluency measurements showed the signal dependence was within the linear regime. After passing through the sample, the probe was dispersed in a monochromator and onto a 64 pixel multichannel MCT array (Infrared Associates).

DFT Calculations. In order to help assign spectral features and interpret the nature of the tIR signal, DFT calculations were carried out using the Gaussian⁵ electronic structure software package revision B01, on an InP nanocluster capped with acetate ligands. The cluster was constructed using the X-ray crystallographic data for a phenylacetate-capped nanocluster⁶ and replacing the phenyl groups with acetyl groups for reduced computational requirements. The

ground state geometry optimization was performed using the HSE06 ⁷⁻⁹ range-separated hybrid DFT functional with the LANL2DZ basis set, with associated basis functions, ¹⁰⁻¹¹ the geometry was considered optimized when both the forces (maximum and RMS force, 0.00050 and 0.000300 Hartree/Bohr, respectively) and displacement (maximum and RMS displacement, 0.0018 and 0.0012 Bohr, respectively) for all atoms were below the threshold criteria. This level of theory has been shown to be accurate for the description of the electronic structure and UV/Vis spectra of pure and doped InP nanoclusters.^{6, 12-13} TDDFT within the Linear-Response framework ¹⁴⁻¹⁶ was then used to calculate the energy gradient of the first excited state, and the structure optimized under this excitation. The Hessian for both the optimized ground and excited state geometries were then calculated to obtain the IR spectra, with the change in transmittance being plotted by subtracting the two spectra as a function of frequency vs intensity (see manuscript Figure 3a). A linear shift of 55 cm⁻¹ was applied to overlap the calculated spectrum with the experimentally obtained FTIR

FIGURES.

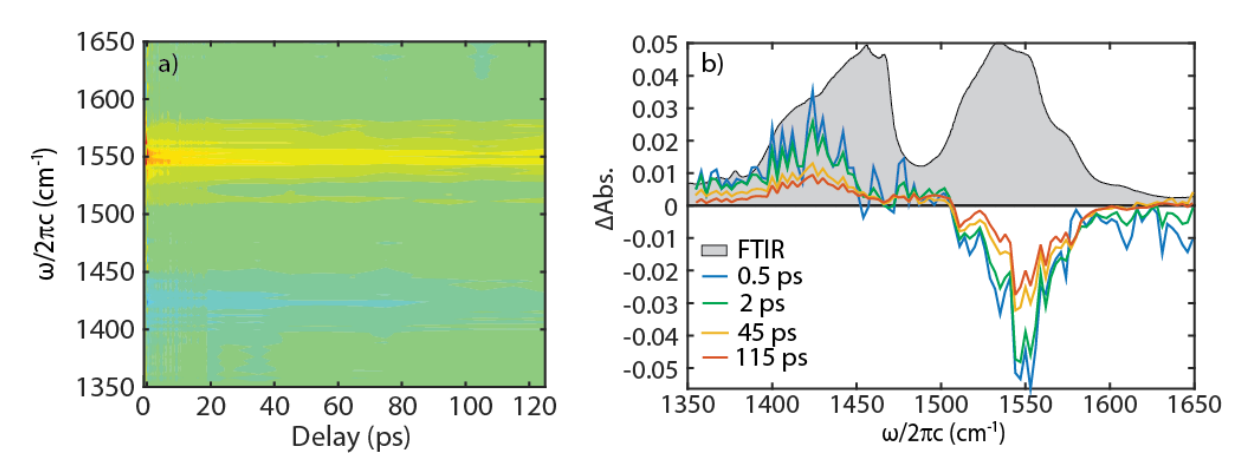


Figure S1 – tIR time dynamics. a) The tIR measurements show a strong negative feature centered around 1550 cm⁻¹ and a positive feature centered at 1425 cm⁻¹. The features persists throughout the timescale of the measurements. b) Comparing the frequency slices at 500 fs, 2 ps, 45 ps, and 115 ps shows no noticeable spectral evolution.

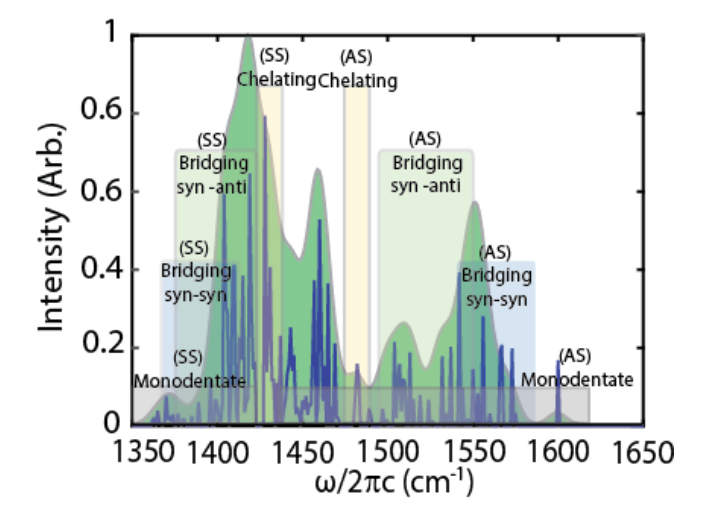


Figure S2 – peak assignment of calculated normal modes showing that the splitting follows the trends experimentally measured by Zeleňák, V. et al. 1

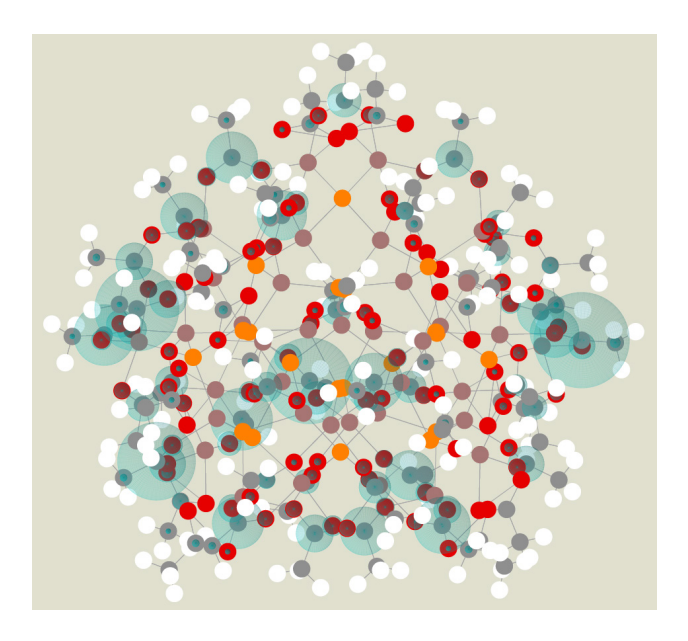


Figure S3 – concentration of normal mode oscillators (blue highlights) related to the vibrational mode centered at 1556 cm⁻¹.

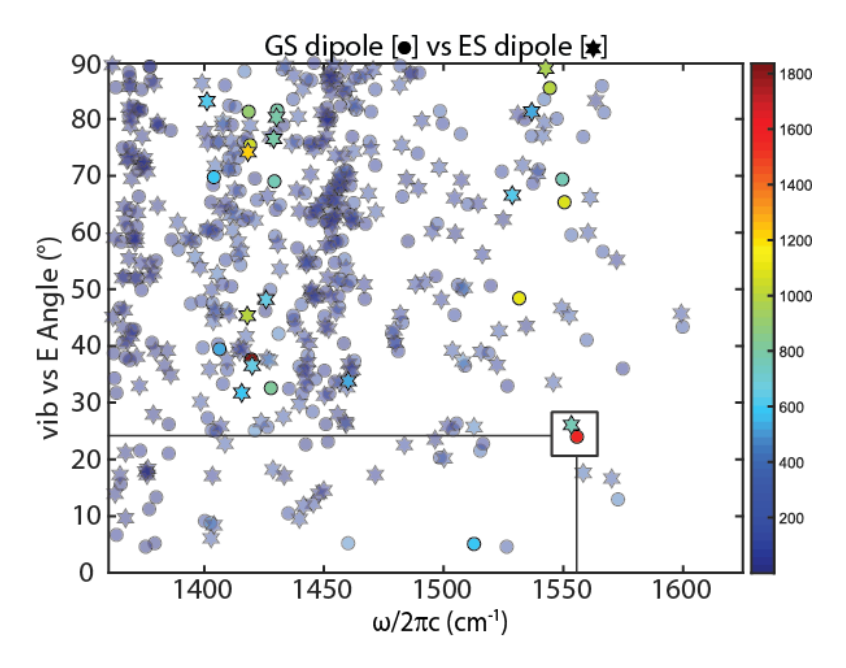


Figure S4 – Scatter plot of calculated vibrational frequencies vs. angle between the vibrational dipole moment and electronic dipole moment for the excited electronic transition. Cool (blue) colors are associated with weak transition dipole moments and the warmer colors (red) reflect the stronger transition dipole moments; the circles (stars) denote ground (excited) state vibrational modes. Focusing on the dipole centered at 1556 cm⁻¹, highlighted by the inset square, there is a clear decrease in intensity where the initial dipole moment drops from 1,567 KM/Mole (red dot) to 750 KM/Mole (teal star) with no appreciable shift in frequency or angle.

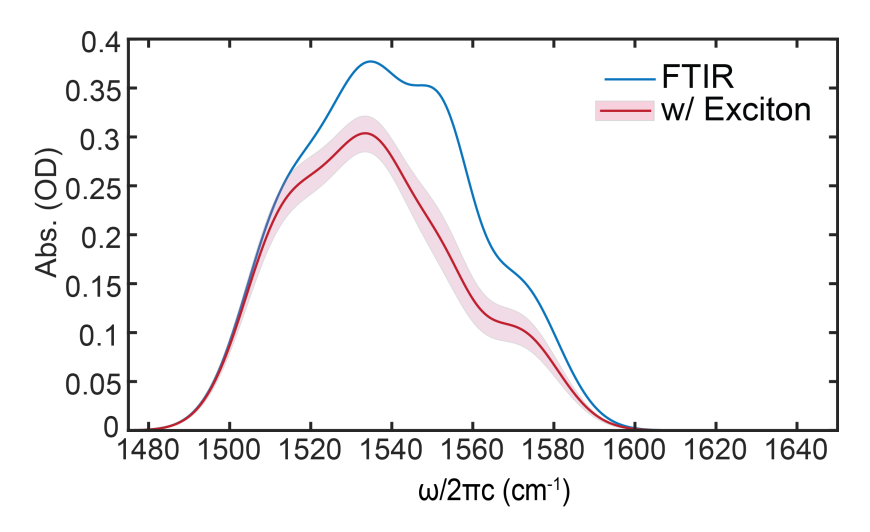


Figure S5- The extracted IR spectrum (red line) in the presence of the exciton overlaid with the FTIR spectrum (blue Line) in the asymmetric carbonyl stretch region, and its associated error (red area). An overall reduction in the extinction coefficients are seen, where there is a significant reduction in the 1550 cm⁻¹ region.

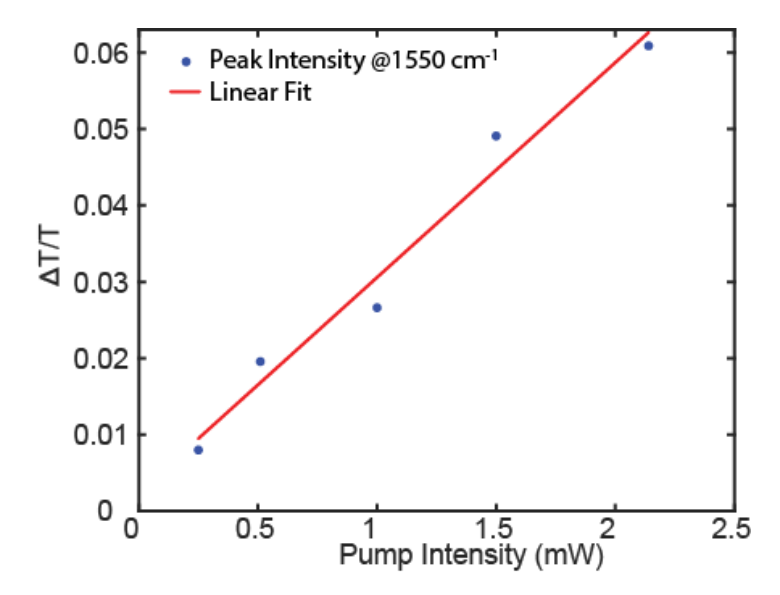


Figure S6 – Pump fluence measurements done for InP-OA centered on the peak at 1550 cm⁻¹ showing a linear trend between .25 and 2.25 mW pump power.

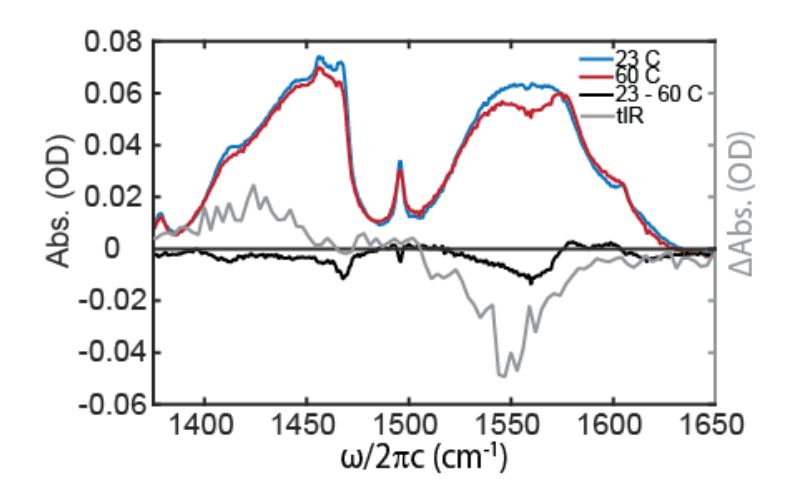


Figure S7 – FTIR showing the difference between the carboxylate region at room temperature (22 C) and 60 C (black line), overlaid with the difference signal seen in the tIR measurements (Gray line). The FTIR at 22 C is shown in blue and the FTIR at 60 C in red.

REFERENCES.

- 1. Zelenak, V.; Vargova, Z.; Gyoryova, K., Correlation of infrared spectra of zinc(II) carboxylates with their structures. *Spectrochim. Acta A* **2007**, *66* (2), 262-72.
- Gary, D. C.; Terban, M. W.; Billinge, S. J. L.; Cossairt, B. M., Two-Step Nucleation and Growth of InP Quantum Dots via Magic-Sized Cluster Intermediates. *Chem. Mater.* 2015, 27 (4), 1432-1441.
- 3. Park, N. M., M.; Ritchhart, A.; Friedfeld, M. R.; Cossairt, B. M., Synthesis of In37P20(O2CR)51 Clusters and Their Conversion to InP Quantum Dots. *Journal of Visualized Experiments* **2019**.
- 4. Lu, C.-H.; Tsou, Y.-J.; Chen, H.-Y.; Chen, B.-H.; Cheng, Y.-C.; Yang, S.-D.; Chen, M.-C.; Hsu, C.-C.; Kung, A. H., Generation of intense supercontinuum in condensed media. *Optica* **2014**, *I* (6), 400.
- 5. Frisch, M. J.; Trucks, G. W.; Schlegel, H. B.; Scuseria, G. E.; Robb, M. A.; Cheeseman, J. R.; Scalmani, G.; Barone, V.; Petersson, G. A.; Nakatsuji, H.; Li, X.; Caricato, M.;

- Marenich, A. V.; Bloino, J.; Janesko, B. G.; Gomperts, R.; Mennucci, B.; Hratchian, H. P.; Ortiz, J. V.; Izmaylov, A. F.; Sonnenberg, J. L.; Williams-Young, D.; Ding, F.; Lipparini, F.; Egidi, F.; Goings, J.; Peng, B.; Petrone, A.; Henderson, T.; Ranasinghe, D.; Zakrzewski, V. G.; Gao, J.; Rega, N.; Zheng, G.; Liang, W.; Hada, M.; Ehara, M.; Toyota, K.; Fukuda, R.; Hasegawa, J.; Ishida, M.; Nakajima, T.; Honda, Y.; Kitao, O.; Nakai, H.; Vreven, T.; Throssell, K.; J. A. Montgomery, J.; Peralta, J. E.; Ogliaro, F.; Bearpark, M. J.; Heyd, J. J.; Brothers, E. N.; Kudin, K. N.; Staroverov, V. N.; Keith, T. A.; Kobayashi, R.; Normand, J.; Raghavachari, K.; Rendell, A. P.; Burant, J. C.; Iyengar, S. S.; Tomasi, J.; Cossi, M.; Millam, J. M.; Klene, M.; Adamo, C.; Cammi, R.; Ochterski, J. W.; Martin, R. L.; Morokuma, K.; Farkas, O.; Foresman, J. B.; Fox, D. J. *Gaussian 16*, Revision B.01; Gaussian Inc.: Wallingford, CT, 2018.
- 6. Gary, D. C.; Flowers, S. E.; Kaminsky, W.; Petrone, A.; Li, X.; Cossairt, B. M., Single-Crystal and Electronic Structure of a 1.3 nm Indium Phosphide Nanocluster. *J. Am. Chem. Soc.* **2016**, *138* (5), 1510-3.
- 7. Vydrov, O. A.; Heyd, J.; Krukau, A. V.; Scuseria, G. E., Importance of short-range versus long-range Hartree-Fock exchange for the performance of hybrid density functionals. *J. Chem. Phys.* **2006**, *125* (7), 074106.
- 8. Heyd, J.; Scuseria, G. E., Efficient hybrid density functional calculations in solids: assessment of the Heyd-Scuseria-Ernzerhof screened Coulomb hybrid functional. *The J. Chem. Phys.* **2004**, *121* (3), 1187-92.
- 9. Scuseria, J. H. G. E., Hybrid functionals based on a screened Coulomb potential. *J. Chem. Phys.* **2003**, *118* (18).

- 10. Wadt, W. R.; Hay, P. J., Ab initio effective core potentials for molecular calculations.

 Potentials for main group elements Na to Bi. *J. Chem. Phys.* **1985**, *82* (1), 284-298.
- 11. Hay, P. J.; Wadt, W. R., Ab initio effective core potentials for molecular calculations.

 Potentials for the transition metal atoms Sc to Hg. *J. Chem. Phys.* **1985**, *82* (1), 270-283.
- Stein, J. L.; Steimle, M. I.; Terban, M. W.; Petrone, A.; Billinge, S. J. L.; Li, X.; Cossairt,
 B. M., Cation Exchange Induced Transformation of InP Magic-Sized Clusters. *Chem. Mater.* 2017, 29 (18), 7984-7992.
- 13. Gary, D. C.; Petrone, A.; Li, X.; Cossairt, B. M., Investigating the role of amine in InP nanocrystal synthesis: destabilizing cluster intermediates by Z-type ligand displacement. *Chem. Commun.* **2016**, *53* (1), 161-164.
- 14. Dreuw, A.; Head-Gordon, M., Single-reference ab initio methods for the calculation of excited states of large molecules. *Chem Rev* **2005**, *105* (11), 4009-37.
- 15. Stratmann, R. E.; Scuseria, G. E.; Frisch, M. J., An efficient implementation of time-dependent density-functional theory for the calculation of excitation energies of large molecules. *J. Chem. Phys.* **1998**, *109* (19), 8218-8224.
- 16. Chong, D. P., Recent Advances in Density Functional Methods (Part 1). World Scientific: 1995; Vol. 1.